

Optimal thermoelectricity with quantum spin-Hall edge states

Daniel Gresta,¹ Mariano Real,² and Liliana Arrachea¹

¹*International Center for Advanced Studies, ECyT-UNSAM,
Campus Miguelete, 25 de Mayo y Francia, 1650 Buenos Aires, Argentina*

²*Instituto Nacional de Tecnología Industrial, INTI,
Av. General Paz 5445, (1650) Buenos Aires, Argentina*

We study the thermoelectric properties of a Kramer's pair of helical edge states of the quantum spin Hall effect coupled to a nanomagnet with a component of the magnetization perpendicular to the direction of the spin-orbit interaction of the host. We show that the transmission function of this structure has the desired qualities for optimal thermoelectric performance in the quantum coherent regime. For a single magnetic domain there is a power generation close to the optimal bound. In a configuration with two magnetic domains with different orientations, pronounced peaks in the transmission functions and resonances lead to a high figure of merit. We provide estimates for the fabrication of this device with HgTe quantum-well topological insulators.

Introduction. Thermoelectricity in the quantum regime is attracting high interest for some years now [1, 2]. Systems hosting edge states, like the quantum Hall and quantum spin Hall are paradigmatic realizations of quantum coherent transport. Several theoretical and experimental results on heat transport and thermoelectricity in these systems have been recently reported [3–31].

Unlike the quantum Hall state, which is generated by a strong magnetic field, the quantum spin Hall (QSH) state taking place in two-dimensional (2D) topological insulators (TI), preserves time-reversal invariance. Therefore, the edge states appear in helical Kramer's pairs [32–37] with opposite spin orientations determined by the spin orbit of the TI. Several heat engines and refrigerators have been recently proposed, taking advantage of the fundamental chiral nature of the quantum Hall edge states, which manifests itself in multiple-terminal structures[19] and in quantum interference[20, 21]. Recently, the property of charge fractionalization was also pointed out as a mechanism to enhance thermoelectricity [23]. All these setups rely on the existence of quantum point contacts and quantum dots in the structure, tunnel-coupled to the edge states, which are generated by recourse to constrictions. The fabrication of these elements is nowadays normal in the context of the quantum Hall effect [38–40]. However, their realization in the context of the QSH effect remains an experimental challenge so far [41], although they are widely investigated theoretically [42–51].

In the quantum coherent regime the electronic transport properties take place without inelastic scattering and are fully characterized by a transmission function. Particle-hole symmetry breaking is a necessary condition for steady-state heat to work conversion. Having transmission functions rapidly changing in energy within the relevant transport window, is the key to achieve optimal thermoelectricity [2, 52–55]. The optimal performance is usually quantified by the *figure of merit* ZT , with the Carnot limit achieved for $ZT \rightarrow \infty$. This ideal limit can be realized for transmission functions containing delta-function like peaks [52]. In this sense, structures with resonant levels like quantum dots are particularly promis-

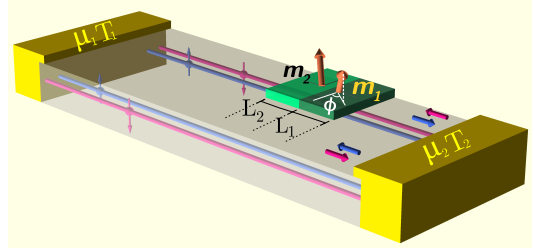


FIG. 1. Sketch of the setup scheme. 2D TI contacted to ohmic contacts at which a bias voltage $eV = \mu_1 - \mu_2$ and temperature difference $\Delta T = T_2 - T_1$ are applied. Two nanomagnets with magnetic moments \mathbf{m}_1 and \mathbf{m}_2 and lengths L_1 and L_2 , are contacted to a helical Kramer's pair of edge states.

ing [56–62]. On another hand, electrical *power generation* out of heat is the aim of thermoelectric heat engines. This is optimized by transmission functions behaving like Heaviside-theta functions within the relevant transport window [54, 55]. In the case of quantum-Hall edge states, configurations with several quantum point contacts and quantum capacitors, have been recently proposed to engineer the transmission function for optimal thermoelectricity by recourse to quantum interference [20].

In the present work we analyze a very different mechanism for edge-state thermoelectricity in a QSH structure. It is based on the coupling of a Kramers pair of helical edge states of the QSH to a magnetic domain. The structure we analyze is sketched in Fig.1, where an edge-state pair of a 2D TI is contacted by nanomagnets. We consider two configurations, a single magnetic island with a given magnetic orientation, as well as two attached islands with different orientations of the magnetic moments. In both configurations, the key ingredient is a finite component of the magnetic moments perpendicular to the direction of the spin-orbit interaction of the TI. A similar structure was previously considered in Refs. 63–65, focusing on the interplay between spin-torque induced current and the consequent pumping induced by the precession of the magnetic moment. In combination to superconducting contacts, this structure has been in-

vestigated as a platform to realize topological superconductivity [66–68]. Here, we show that the simple two-terminal setup of Fig.1, under the effect of a simultaneous voltage and temperature biases, has the desired properties for optimal heat to electrical work dc conversion. We analyze the transmission function for this structure and the impact of its different features on the thermoelectric response. Remarkably, this function takes the best of the two worlds regarding power generation and large figure of merit, since it has features alike a theta function and delta-function type resonances due to bound states in the gap, as well as peaks alike quantum dots. We provide estimates for the different components of the device and we argue that it is within the present state of the art of fabrication of 2D TI structures [35–37].

Thermoelectric performance in the quantum coherent regime. We briefly review the linear-response thermoelectric approach assuming small differences of chemical potential $eV = \mu_1 - \mu_2$ (with $\mu_1 = \mu$), and temperature $\Delta T = T_2 - T_1$ (with $T_1 = T$), applied at the contacts of the edge states, as indicated in Fig. 1 [2]. The induced charge and heat currents are

$$\begin{pmatrix} I^C/e \\ I^Q \end{pmatrix} = \begin{pmatrix} \mathcal{L}_{11} & \mathcal{L}_{12} \\ \mathcal{L}_{21} & \mathcal{L}_{22} \end{pmatrix} \begin{pmatrix} X_1 \\ X_2 \end{pmatrix}. \quad (1)$$

We have introduced the affinities $X_1 = eV/k_B T$ and $X_2 = \Delta T/k_B T^2$. In the quantum coherent regime, the elements of the Onsager matrix are fully determined by the transmission function $\mathcal{T}(\varepsilon)$ as follows,

$$\mathcal{L}_{ij} = -T \int \frac{d\varepsilon}{h} \frac{\partial f(\varepsilon)}{\partial \varepsilon} (\varepsilon - \mu)^{i+j-2} \mathcal{T}(\varepsilon), \quad (2)$$

where $f(\varepsilon) = 1/(e^{(\varepsilon - \mu)/k_B T} + 1)$. The key for the thermoelectric heat to work conversion is encoded in the off-diagonal coefficient $\mathcal{L}_{12} = \mathcal{L}_{21}$. The quality of this conversion is evaluated in terms of the efficiency (for the heat engine), $\eta^{\text{he}} = (I^C T X_1)/I^Q$, being $P = I^C T X_1$ the generated power, or coefficient of performance (for the refrigerator), $\eta^{\text{fri}} = -I^Q/I^C T X_1$, being $-I^Q$ the heat current extracted from the cold reservoir. In both cases, for a given difference of temperature, the maximum values for these coefficients can be parametrized by the figure of merit $ZT = \mathcal{L}_{21}^2/\text{Det}\hat{\mathcal{L}}$, as follows

$$\eta^{\text{max}} = \eta_C^{\text{he/fri}} \frac{\sqrt{ZT+1}-1}{\sqrt{ZT+1}+1}, \quad (3)$$

being $\eta_C^{\text{he}} = [\eta_C^{\text{fri}}]^{-1} = \Delta T/T$ the Carnot efficiency, which is achieved for $ZT \rightarrow \infty$, while the value $\eta^{\text{he/fri}} \sim 0.3 \eta_C$ corresponds to $ZT \sim 3$. As originally shown by Mahan and Sofo, the ideal upper bound $\eta_C^{\text{he/fri}}$ is obtained for $\mathcal{T}(\varepsilon) \sim \delta(\varepsilon - \varepsilon_0)$, while ZT attains high values when $\mathcal{T}(\varepsilon)$ has peaks within the relevant transport window $|\varepsilon - \varepsilon_0| \sim k_B T$. On another hand, for the heat engine operational mode, the maximum achievable power for a given ΔT and the corresponding efficiency are

$$P_{\text{max}} = \eta_C \frac{\mathcal{L}_{12}^2 X_2}{4\mathcal{L}_{11}}, \quad \eta(P_{\text{max}}) = \eta_C \frac{ZT}{2(ZT+2)}. \quad (4)$$

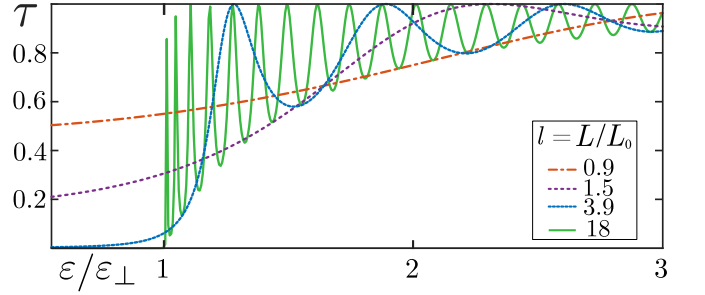


FIG. 2. Transmission function $\mathcal{T}(\varepsilon)$ defined in Eq. 8 within a range of lengths l for an island with homogeneous magnetic moment. Energies are expressed in units of $\varepsilon_{\perp} = Jm_{\perp}$, lengths are expressed in units of $L_0 = \varepsilon_{\perp}/\hbar v_F$.

It has been shown that the maximum power is bounded by $0.32P_0$ for a transmission function of the form $\mathcal{T}(\varepsilon) \sim \theta(\varepsilon - \mu - \varepsilon_0)$, where $P_0 = (k_B \Delta T)^2/h$ [54].

Transmission function. The structure sketched in Fig.1 is modeled by the following Hamiltonian

$$H = \int dx \Psi^{\dagger}(x) [(-i\hbar v_F \partial_x) \hat{\sigma}_z + J\mathbf{m}(x) \cdot \hat{\boldsymbol{\sigma}}] \Psi(x), \quad (5)$$

where $\Psi(x) = (\psi_{R,\uparrow}(x), \psi_{L,\downarrow}(x))^T$, represent the right(left)-moving electrons with velocity v_F and \uparrow (\downarrow) spin orientations, J is the magnetic exchange interaction between the magnetic moment of the island and the spin of the electrons, and $\hat{\boldsymbol{\sigma}} = (\hat{\sigma}_x, \hat{\sigma}_y, \hat{\sigma}_z)$ are the Pauli matrices. The magnetic island is described by the following piece-wise spacial distribution of the magnetic moment within segments of lengths $L_j = x_j - x_{j-1}$.

$$\mathbf{m}(x) = \sum_{j=1}^N \theta(x_j - x) \theta(x - x_{j-1}) \mathbf{m}_j. \quad (6)$$

$\mathbf{m}_j = (m_{j\perp} \cos \phi_j, m_{j\perp} \sin \phi_j, m_{j\parallel})$ is the magnetic moment per unit length with components $m_{j\parallel}$ (parallel) and $m_{j\perp}$ (perpendicular) with respect to the direction of the spin-orbit interaction of the TI. We focus on a single island ($N = 1$) and two islands $N = 2$ of the same length but with different orientations of the magnetic moment.

In order to calculate the transmission function we proceed as in Ref. [69], starting from the evolution operator in space for the whole scattering region. It reads $\hat{\mathcal{U}}(x_N, x_0) = \prod_{j=1}^N \hat{\mathcal{U}}(x_j, x_{j-1})$, with

$$\begin{aligned} \hat{\mathcal{U}}(x_j, x_{j-1}) &= \exp\left\{i \frac{\varepsilon_{j\parallel}}{\hbar v_F} L_j\right\} \exp\{-i\boldsymbol{\lambda}_j \cdot \hat{\boldsymbol{\sigma}}\} \\ &= \exp\left\{i \frac{\varepsilon_{j\parallel}}{\hbar v_F} L_j\right\} [\hat{\sigma}_0 \cos \lambda_j - i\mathbf{n}_j \cdot \hat{\boldsymbol{\sigma}} \sin \lambda_j], \end{aligned} \quad (7)$$

being $\boldsymbol{\lambda}_j = (i \varepsilon_{j\perp} \sin \phi_j, -i \varepsilon_{j\perp} \cos \phi_j, \varepsilon) L_j/(\hbar v_F)$, with $\varepsilon_{\parallel,\perp} = Jm_{\parallel,\perp}$, and $\mathbf{n}_j = \boldsymbol{\lambda}_j/\lambda_j$. The transmission function is the inverse of the element 2, 2 of the transfer matrix, which is, in turn, the inverse of the matrix $\hat{\mathcal{U}}(L, 0)$. Hence, $\mathcal{T}(\varepsilon) = |\text{Det}[\hat{\mathcal{U}}(x_N, x_0)]/\mathcal{U}(x_N, x_0)_{1,1}|^2$.

Single homogeneous island. We start by discussing the case of an homogeneous domain of length L , described by the previous Hamiltonian with a single piece, $N = 1$. The resulting transmission function is

$$\mathcal{T}(\varepsilon) = \frac{|\varepsilon_{\perp}^2 - \varepsilon^2|}{|\varepsilon_{\perp}^2 - \varepsilon^2| \cos^2 \lambda + \varepsilon^2 \sin^2 \lambda}, \quad (8)$$

being $\lambda = rl$, with $l = L/L_0$, $L_0 = \hbar v_F/\varepsilon_{\perp}$ and $r = \sqrt{(\varepsilon/\varepsilon_{\perp})^2 - 1}$. Notice that the transmission function does not depend on the detailed orientation of the magnetic moment but only on the projection m_{\perp} perpendicular to the direction of the spin-orbit interaction of the material. It is also symmetrical to $\varepsilon = 0$. The latter introduces an effective coupling between the two Kramer's partners, that may open a gap in the spectrum of magnitude ε_{\perp} .

The behavior of $\mathcal{T}(\varepsilon)$ is illustrated in Fig.2, where we see its dependence on the length of the island. For short islands, there is a sizable tunneling amplitude through the magnetic island, while as the length of the magnet increases, the transmission function tends to a step function close to $\varepsilon \sim \varepsilon_{\perp}$. We get the following behavior of the transmission function at the opening of the gap as a function of length $\mathcal{T}(\varepsilon_{\perp}) = [1 + l^2]^{-1}$, with $l = L/L_0$, while the slope behaves as $d\mathcal{T}/d\varepsilon|_{\varepsilon_{\perp}} = 2l^4[1 + l^2]/3[1 + l^2]^3$, which saturates at the value of $2/3$, for increasing l . For energies $\varepsilon > \varepsilon_{\perp}$, $\mathcal{T}(\varepsilon)$ exhibits oscillations with maxima $\mathcal{T}^{\max}(\varepsilon_n) = 1$ and minima $\mathcal{T}^{\min}(\varepsilon_m) = 1 - (\varepsilon_{\perp}/\varepsilon_m)^2$ at energies satisfying $(\varepsilon_{n(m)})^2 = (\varepsilon_{\perp})^2 + (\pi\alpha_{n(m)}\hbar v_F/L)^2$, with $\alpha_{n(m)}$ being an integer (half-integer) number, respectively.

The impact of the transmission function on the thermoelectric performance of the heat engine is illustrated in Fig. 3 for two lengths of the magnetic domain, in a range of chemical potentials close to the edge of the energy gap, within a temperature range scaled by the reference temperature $T_0 = \varepsilon_{\perp}/k_B$. For the shortest length shown in panels (a) and (b), $l = 10$, $\mathcal{T}(\varepsilon_{\perp}) < 0.01$ and $d\mathcal{T}/d\varepsilon|_{\varepsilon_{\perp}} \sim 0.65$, i.e. close to the maximal slope ($2/3$), implying a pronounced step in the transmission function at the closing of the energy gap. The plots shown in Figs.(c) and (d) correspond to a longer island of length $l = 20$, for which the step function is slightly more pronounced. For very low temperatures, within a scale $k_B T$ smaller than the width of the peaks of $\mathcal{T}(\varepsilon)$, both P_{\max} and ZT vanish for $\mu = \varepsilon_n$ (see arrows in panels (a) and (b)). As the temperature increases, the behavior of these quantities is ruled by the effect of several peaks. At sufficiently high temperature, such that several maxima of $\mathcal{T}(\varepsilon)$ are included in an energy window of width $k_B T$, the behavior is dominated by the average between the envelopes for the minima and the maxima of $\mathcal{T}(\varepsilon)$. The resulting function is approximately a smoothed step-function, independently of the length of the island. For this reason, P_{\max} shows a wide maximum centered at $\sim |\varepsilon_{\perp} - \mu| \sim k_B T$ [20, 54]. The maximum is as high

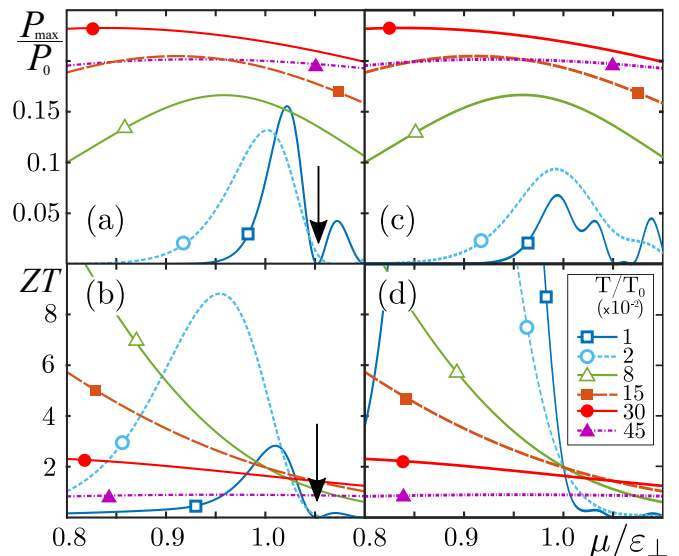


FIG. 3. Maximum power (upper panels) and figure of merit ZT (lower panels), for a single magnetic domain of $l = 10$ (a)-(b) and $l = 20$ (c)-(d). The maximum values in (a) and (b) are $P_{\max}(T = 0.3) = 0.240P_0$ (a), $ZT(T = 0.08) = 60$ (b), $P_{\max}(T = 0.45) = 0.244P_0$ (c), and $ZT(T = 0.02) = 274$ (d). The temperatures are expressed in units of $T_0 = \varepsilon_{\perp}/k_B$ and the power is expressed in units of $P_0 = (k_B \Delta T)^2/h$. Other details are the same as in Fig.2.

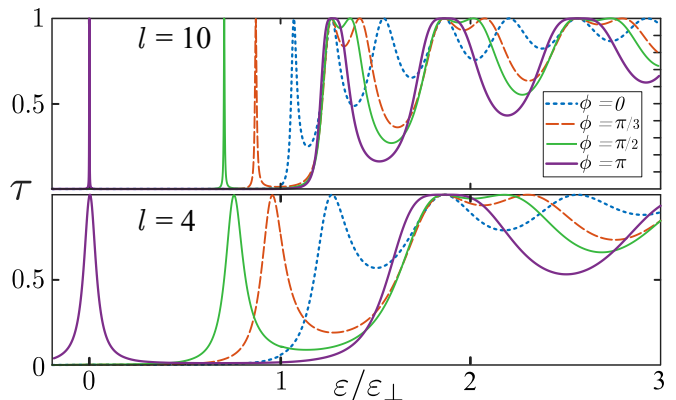


FIG. 4. Transmission function $\mathcal{T}(\varepsilon)$ defined in Eq. 8 for two magnetic domains of equal size ($l = 4, 10$) with the perpendicular component of the magnetic moments oriented with a relative tilt ϕ .

as $\sim 0.244P_0$, i.e. $\sim 75\%$ of the bound $0.32P_0$. $\mathcal{T}(\varepsilon)$ is symmetric with respect to $\varepsilon = 0$ and has a well of unit depth and width $\sim 2\varepsilon_{\perp}$. This feature dominates the behavior of the power and ZT at high temperatures. These properties depend mildly on the length of the island. Details of the effect of the different features of $\mathcal{T}(\varepsilon)$ on the thermoelectric response as a function of T are presented in the supplementary material (SM) [72].

Two domains. We now turn to analyze the case where we have two pieces, corresponding to $N = 2$ in Eq.(7) with $L_1 = L_2 = L$, $\phi_1 = 0$, $\phi_2 = \phi$, and $\varepsilon_{\perp,1} = \varepsilon_{\perp,2} =$

ε_{\perp} . The resulting transmission function reads,

$$\mathcal{T}(\varepsilon) = \left\{ \left[\cos^2 \lambda + \frac{\sin^2 \lambda}{r^2} \left(\cos \phi - \frac{\varepsilon^2}{\varepsilon_{\perp}^2} \right) \right]^2 + \left[-\frac{\varepsilon}{\varepsilon_{\perp}} \frac{\sin 2\lambda}{r} + \sin \phi \frac{\sin^2 \lambda}{r^2} \right]^2 \right\}^{-1}. \quad (9)$$

The new feature in the present case, in comparison to the case of a single magnetic moment, is the existence of resonances within the gap, $|\varepsilon| < \varepsilon_{\perp}$, for $\phi \neq 0$. The position of the resonant state depends on the phase difference ϕ . For $\phi = \pi$, Eq. (5) coincides in that case with the model introduced by Jackiw and Rebbi [70, 71], which has a topological zero mode localized at the domain wall boundary. In Ref. 72 we analyze the impact of the length of the domains on the width of the resonant state. We also show that this feature is robust under weak disorder in the length of the domains and the orientation of the magnetization along each domain.

The behavior of the transmission function for two domains is illustrated in Fig. 4 for a set of orientations. The upper and lower panels show the transmission function for $l = 10$ and $l = 4$ for each domain, respectively. Note that the width of the resonance decreases for increasing l . The corresponding thermoelectric response is shown in Fig. 5. Close to the edge of the gap, the minima of $\mathcal{T}(\varepsilon)$ for $\phi = \pi$, are deeper than the ones for a single domain (see Eq. 6 of Ref. 72). Notice that the latter corresponds to a single domain with total length $2L$. On the other hand, for $\phi = \pi$, the energy difference between peaks is twice the one for $\phi = 0$. Hence, for two domains with $\phi = \pi$, the first peak after the closing of the gap is expected to generate a thermoelectric response with a high figure of merit, similar to that of a Lorenzian function within a range of temperatures larger than in the case of a single ferromagnetic one. For $\mu \sim k_B T$ the thermoelectric response is dominated by the resonance within the gap. This leads to high values of ZT for $k_B T \lesssim 10\gamma$, being γ the width of the resonance, which depends on the domain length. These details are discussed in Ref. [72]. For higher temperatures, the transport behavior is dominated by the Heaviside-step function and well-shaped envelopes of the transmission function, and the thermoelectric response is similar to the one discussed for a single domain.

Conclusions. We have analyzed the transmission function characterizing the coherent transport of electrons in a structure consistent of a pair of helical edge states of a 2D TI coupled by a magnetic island with a magnetic moment having a component perpendicular to the direction of the spin orbit of the TI. We have shown that this setup has the necessary conditions to achieve high performance thermoelectricity. The key is the opening of a gap in the spectrum of the helical edges with a steep increase of the transmission function at the opening of the propagating modes in the spectrum. Depending on

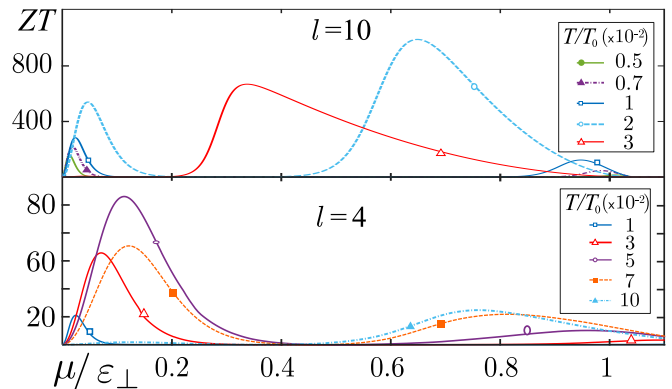


FIG. 5. Figure of merit ZT for two magnetic domains of length $l = 4, 10$, with the perpendicular component of the magnetic moments tilted in $\phi = \pi$. Other details are similar to previous figures.

the energy range and the configuration of the magnetic domains, the transmission function has features akin to a theta-function, as well as with features akin to a delta-function, which are known to be optimal for high-power production and figure of merit, respectively. Due to the resonant states in the gap for two magnetic domains, very large values of the figure of merit, $ZT > 100$, are attained for the heat-engine and refrigeration modes. Our calculations focus on a single pair of edge states, but the currents simply scale in a factor two when the pair at the opposite edge is also considered. The range of operation is set by the magnetic gap ε_{\perp} . For a single domain generating an effective magnetic field of $\sim 1.8 - 4$ T [73], we estimate $\varepsilon_{\perp} \sim 1 - 2 \times 10^{-4} eV$, corresponding to reference temperatures $T_0 \sim 1.2 - 2.4$ K. According to our study, such a device with a length of the magnetic island of $\sim 10L_0$, being $L_0 = \varepsilon_{\perp}/\hbar v_F$, operates as a heat engine at a high performance ($\sim 75\%$ of the optimal bound) regarding power generation with a figure of merit $ZT \gg 1$ for $T < 0.5T_0$. Taking estimates for the Fermi velocity of the helical edge states in quantum wells of HgTe from Ref. [35], we have $\hbar v_F \sim 0.9 eV/nm$, leading to $L_0 \sim 10 - 20 \mu m$. These parameters are at the state of the art of present experimental realizations.

Acknowledgements. We thank A. Aligia and P. Roura-Bas for carefully reading our manuscript and useful comments. We acknowledge support from CONICET, Argentina. We are sponsored by pip-rd 20141216-4905 of CONICET, PICT-2014-2049 and PICT-2017-2726 from Argentina, as well as the Alexander von Humboldt Foundation, Germany (LA).

SUPPLEMENTAL MATERIAL: OPTIMAL THERMOELECTRICITY WITH QUANTUM SPIN-HALL EDGE STATES

In order to gain insight on the features of the transmission function $\mathcal{T}(\varepsilon)$ ruling the thermoelectric response of a single Kramer's pair of helical edge states of the QSH coupled to a nanomagnet, we analyze simpler functions and take them as reference. In particular, we analyze the thermoelectric response of Heaviside-step (Sec. A), well-shaped (Sec. B) transmission functions, and a well-shaped transmission function with a resonance in the energy gap (Sec. C). In Sec. II we show that at different energy scales, $\mathcal{T}(\varepsilon)$ for the nanomagnet-QSH system contains ingredients of these different functions. Depending on the temperature, a particular one becomes dominant. We show in Sec. III the existence of a resonant state in the case of two magnetic domains with relative orientation $\phi = \pi$. Finally, in Sec. C we analyze the robustness of the main features of the transmission function against disorder in the orientation of the magnetic moment within the domains.

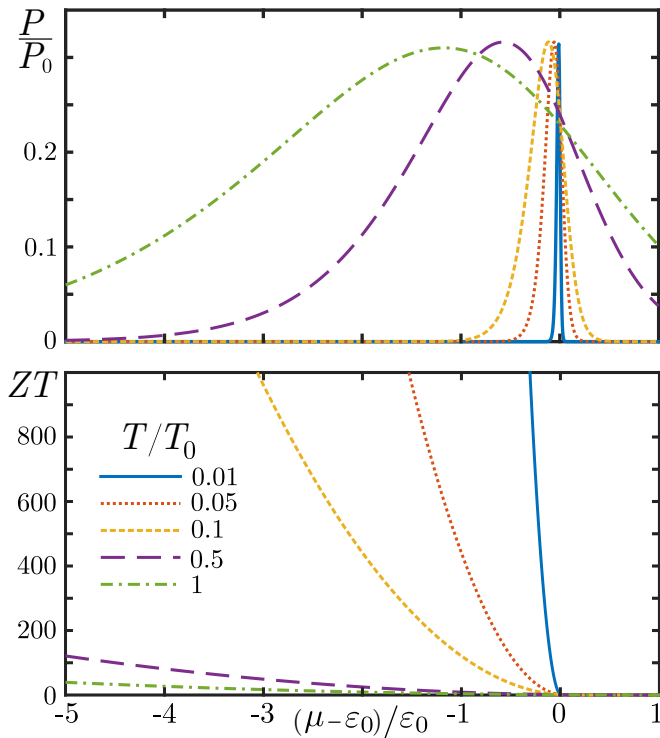


FIG. 6. Maximum power P_{\max} and ZT for the Heaviside step function defined in Eq. (10) for several temperatures, expressed in units of $T_0 = \varepsilon_0/k_B$.

A Heaviside-function

We review the behavior of the figure of merit ZT and the maximum power P_{\max} , defined, respectively, in Eqs. (3) and (4) of the main text, for the case of a transmission

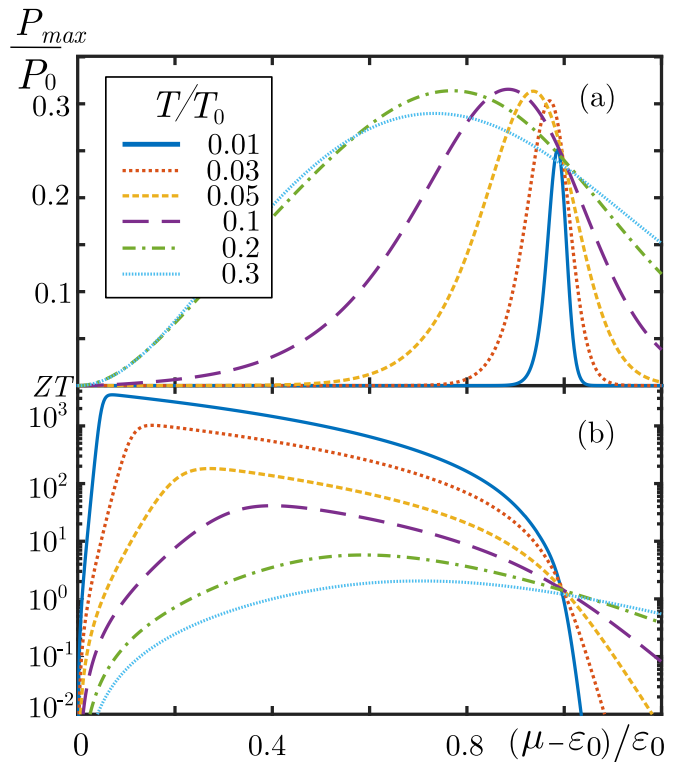


FIG. 7. Maximum power and ZT for a well-function defined in Eq. (11) as function of μ for several temperatures. The functions are symmetric with respect to $\mu = 0$. Other details are the same as in the previous Fig.

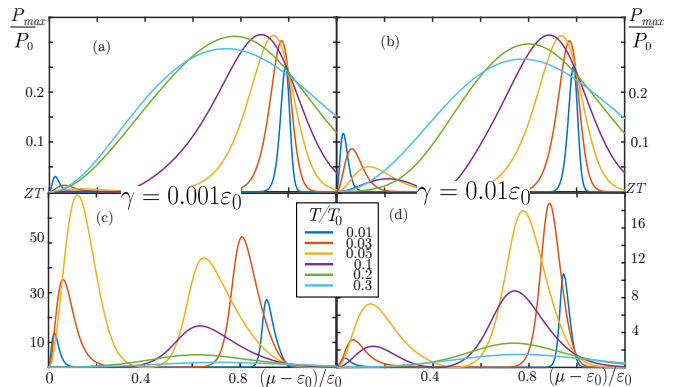


FIG. 8. (a-b) Maximum power and (c-d) ZT for the bound state. (a-c) correspond to $\gamma = 0.001\varepsilon_0$ while (b-d) to $\gamma = 0.1\varepsilon_0$. Other details are the same as in the previous figures.

function with the form of a Heaviside function,

$$\mathcal{T}(\varepsilon) = \theta(\varepsilon - \varepsilon_0). \quad (10)$$

Results are shown in Fig. 6. The upper bound for the maximum achievable power, $0.32P_0$, where $P_0 = (k_B\Delta T)^2/h$, is reached [53, 54] at $\mu - \varepsilon_0 \sim -k_B T$. We see that ZT achieves high values at low temperatures. However, it is a decreasing function of the temperature, and drops very rapidly to $ZT \sim 0$ in the region of $\mu - \varepsilon_0 > 0$, where $\mathcal{T} = 1$.

B Well-shaped function

In this section we consider a well-shaped function of the form

$$\mathcal{T}(\varepsilon) = \theta(\varepsilon - \varepsilon_0) + \theta(-\varepsilon - \varepsilon_0). \quad (11)$$

The range $|\varepsilon| < \varepsilon_0$ behaves like the transmission function of the nanomagnet coupled to the helical edge states within the energy gap for sufficiently large magnets such that $L \gg L_0$. In the range $|\varepsilon| > \varepsilon_0$, it is similar to the envelope for the sequence of maxima of the transmission function of the nanomagnet. Both the maximum power and ZT are even functions of μ . Results are shown in Fig. 7 for $\mu > 0$. For low temperatures, $T < 0.2T_0$, being $T_0 = \varepsilon_0/k_B$, the behavior of both, the maximum power and ZT is similar to that of the two Heaviside-type transmission functions. In fact, we can identify in Fig. 7 the same features that we have already analyzed in Fig. 6. In particular, we see that the maximum power achieves the optimal bound $0.32P_0$. However, for $T > 0.2T_0$, the maximum value becomes a decreasing function of the temperature. The behavior of ZT is similar to that of the step function within the whole range of temperatures.

C Well-shaped transmission function with a resonant peak

We now consider the thermoelectric response of a transmission function, which consists of a well-shaped transmission function with a Lorentzian function of width γ in the center of the well,

$$\mathcal{T}(\varepsilon) = \theta(\varepsilon - \varepsilon_0) + \theta(-\varepsilon - \varepsilon_0) + \frac{\gamma^2}{(\gamma^2 + \varepsilon^2)}. \quad (12)$$

We focus on $\gamma \ll \varepsilon_0$, which is relevant for the description of a transmission function of the nanomagnet with two magnetic domains, which hosts a narrow resonance inside the gap. The corresponding thermoelectric response is presented in Fig. 8 for two different widths of the resonance, $\gamma = 0.001\varepsilon_0$ and $\gamma = 0.01\varepsilon_0$. We start by analyzing the behavior of the maximum power, which is shown in the upper panels of the Fig. By comparing these plots with those shown in the upper panels of Fig. 7 and Fig. 6, we see that the dominant response at all temperatures is due to the well-function feature. For low temperatures $T < 10\gamma/k_B$, we can also identify features originated in the response due to the resonant peak. Concretely, we can identify maxima of P_{\max} at $\mu \sim k_B T$. The maxima are anyway much smaller than the optimal bound ($\sim P_0/3$ for the case of $T = 0.01T_0$ and $\gamma = 0.01$). In the behavior of ZT , we can also identify features originated in the resonance and on the step function. For $T \leq 0.05T_0$, the resonance leads to maxima in ZT at values of the chemical potential that are $|\mu| \propto k_B T$, while the step function leads to maxima of ZT at values of the chemical potential satisfying $|\mu - \varepsilon_0| \propto k_B T$.

Hence, within this low-temperature range, there are two maxima, which become closer one another as the temperature increases. For higher temperature the positions of the two maxima change mildly but the values of ZT decrease rapidly with the temperature.

Appendix A THERMOELECTRIC REGIMES OF THE NANOMAGNET COUPLED TO THE HELICAL EDGE STATES

We expect different thermoelectric regimes as a function of temperature. The transmission function of the nanomagnet coupled to the edge states presents ingredients of the three functions described in the previous section. Concretely, we expect that at low temperatures, where resonances and peaks are resolved, the thermoelectric response resembles that of the Lorentzian function, at higher temperatures, the behavior of the Heaviside function becomes dominant and at even higher temperatures, the well-shape due to the gap causes the decreasing behavior of both P_{\max} and ZT as functions of T for all values of the chemical potential μ .

An overview of the different regimes is presented in Fig. 9. Here, we show the functions $\overline{ZT} = \text{Max}_\mu [ZT]$ and $\overline{P}_{\max} = \text{Max}_\mu [P_{\max}]$, where Max_μ denotes the maximum value of the quantity over the whole range of values of μ . The boundary for the lowest-temperature regime is identified with the range of T below the one corresponding to the minimum of $[P_{\max}]$. This regime is akin to the response due to a Lorentzian-type transmission function and is non-universal, since it depends on the details of the resonant peaks of $\mathcal{T}(\varepsilon)$. The latter are determined by the length of the island and the number of domains. In the case of two domains with $\phi = \pi$, it is possible to distinguish a narrow feature, which is associated to a resonance within the gap, followed by a second feature, associated to the first peak after the closing of the gap. For islands with a single domain, we can distinguish only one feature, which is associated to the first peak after the closing of the gap. For larger temperatures, we enter the regime dominated by the Heaviside-type function corresponding to averaging the envelopes of the minima and maxima of the transmission function for $\varepsilon > \varepsilon_\perp$. While the maxima corresponds to $\mathcal{T} = 1$, the minima are deeper for two domains with $\phi = \pi$ than for a single domain. Hence, the values of $\text{Max}_\mu [P_{\max}]$ within this regime are higher for a single domain than for two antiferromagnetic ones. For both orientations, the behavior is universal, namely, it does not depend on the length of the island. The figure 9 shows the onset of the third (high-temperature) regime, where the well-shape becomes dominant and $\text{Max}_\mu [P_{\max}]$ turns to be a decreasing function of T .

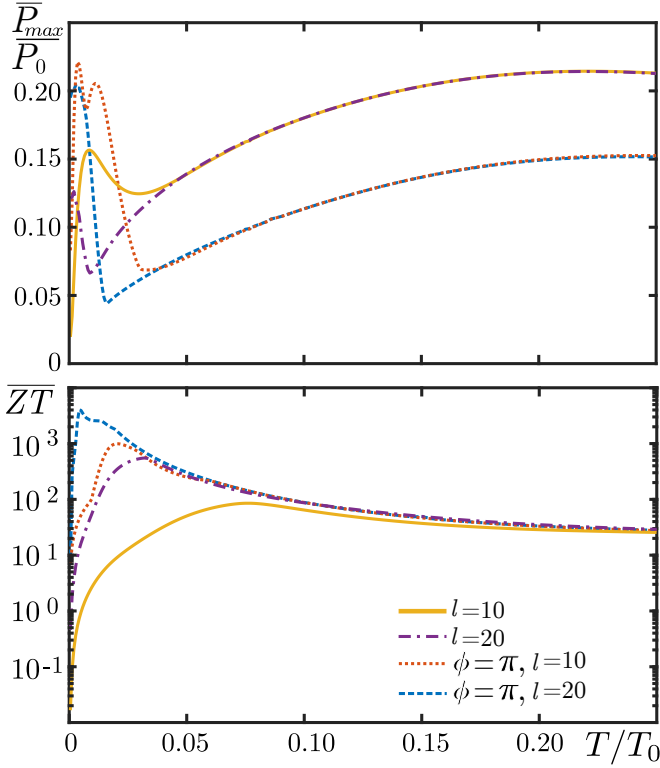


FIG. 9. $\overline{ZT} = \text{Max}_\mu [ZT]$ and $\overline{P}_{\text{max}} = \text{Max}_\mu [P_{\text{max}}]$, corresponding to the maximum values of P_{max} and ZT over the whole range of μ , as functions of the temperature T . AF denotes islands with two domains antiferromagnetically aligned.

Appendix B RESONANT STATE IN THE $\phi = \pi$ CONFIGURATION

The existence of a resonant state in the gap for this configuration can be understood after noticing that the Hamiltonian of Eq. (5) of the main text reduces to a 1D Dirac Hamiltonian with a mass, determined by the coupling to m_\perp , which changes sign at the boundary between the two domains. This is, precisely the model analyzed by Jackiw and Rebbi [70], which is the continuous version of the Su-Schrieffer-Heeger model [71] for polyacetylene. These models are known to host topological zero modes localized at the domain wall. We now analyze the degree of localization of the zero mode for the case of interest, where the length of the magnets (equivalent to the massive region of the Dirac Hamiltonians) is finite.

The inverse of transmission function of two magnetic domains with length L and a relative orientation ϕ of the component of the magnetization perpendicular to the spin-orbit interaction of the TI, takes the following simple form

$$[\mathcal{T}(\varepsilon, l, \phi)]^{-1} = \left[\cos^2 \lambda + \frac{\sin^2 \lambda}{r^2} (\cos \phi - x^2) \right]^2 + \left[-x \frac{\sin 2\lambda}{r} + \sin \phi \frac{\sin^2 \lambda}{r^2} \right]^2, \quad (13)$$

where $l = L/L_0$, $x = \varepsilon/\varepsilon_\perp$, $r = \sqrt{x^2 - 1}$ and $\lambda = lr$. Notice that for $\varepsilon = 0$, the latter function reads

$$\begin{aligned} [\mathcal{T}(0, l, \phi)]^{-1} &= \left[\cos^2(li) + \left(\frac{\sin(li)}{i} \right)^2 \cos \phi \right]^2 + \left(\sin \phi \left(\frac{\sin li}{i} \right)^2 \right)^2 \\ &= \left(\cosh^2 l + \sinh^2 l \cos \phi \right)^2 + \sin^2 \phi \sinh^2 l \\ &= \left(1 + (1 + \cos \phi) \sinh^2 l \right)^2 + \sin^2 \phi \sinh^2 l, \end{aligned} \quad (14)$$

where we see that $\mathcal{T}(0, l, \phi) \sim 0$ for $l > 1$ except for $\phi = (2n+1)\pi$, with n integer, in which case $\mathcal{T}(0, l, (2n+1)\pi) = 1$. Therefore, we conclude that for $\phi = (2n+1)\pi$, there is a resonant state in the center of the gap, with energy $\varepsilon = 0$. The width of this resonant state depends on the length as e^{-l} , which means that the width of the resonance decreases with l .

For this configuration there is a simple expression for the minima of the oscillations above the gap. It reads

$$\mathcal{T}^{\text{min}}(\varepsilon_m) = \left[\frac{(\varepsilon_m^2 - \varepsilon_\perp^2)}{(\varepsilon_m^2 + \varepsilon_\perp^2)} \right]^2, \quad (15)$$

where $(\varepsilon_m)^2 = (\varepsilon_\perp)^2 + (\pi\alpha_m \hbar v_F / L)^2$, with α_m being a half-integer number.

In addition, we estimate the critical length of the domains for the resonant peak to develop. We use the following criterion to determine the critical length l_c for which the width of the resonant state is smaller than the energy gap, $\mathcal{T}(\varepsilon/\varepsilon_\perp = 0.5) \leq 0.5$, leading to

$$\mathcal{T}\left(\frac{\varepsilon}{\varepsilon_\perp} = 0.5, l_c\right) = \frac{9/8}{\frac{15}{8} - \cosh(\sqrt{3}l_c) + \frac{1}{4} \cosh(2\sqrt{3}l_c)}. \quad (16)$$

We get $l_c \simeq 0.9$. Hence, we identify a resonance in the configuration of $\phi = \pi$ for $l > l_c$. We have verified that for angles $\phi \neq \pi$ the criterion does not change significantly and the condition $l > 1$ is enough to clearly resolve a resonant state within the gap.

The previous analysis was based on the assumption that the two domains have the same length. In what follows, we analyze the case of magnetic domains with different lengths, focusing on the situation where one of the domains has $l_1 > 1$ and the second domain has $l_2 \leq l_1$. The generalization of Eq. (9) of the main text to the present case reads

$$\begin{aligned} [\mathcal{T}(\lambda_1, \lambda_2, \phi, x)]^{-1} &= \left[\cos \lambda_1 \cos \lambda_2 + \frac{\sin \lambda_1 \sin \lambda_2}{r^2} (\cos \phi - x^2) \right]^2 \\ &+ \left[\sin \phi \frac{\sin \lambda_1 \sin \lambda_2}{r^2} - \sin(\lambda_1 + \lambda_2) \frac{x}{r} \right]^2. \end{aligned} \quad (17)$$

For $\phi = \pi$, the height of the resonant level is given by

$$\mathcal{T}(\lambda_1, \lambda_2, \phi = \pi, x = 0) = \frac{1}{\cosh(l_1 - l_2)}. \quad (18)$$

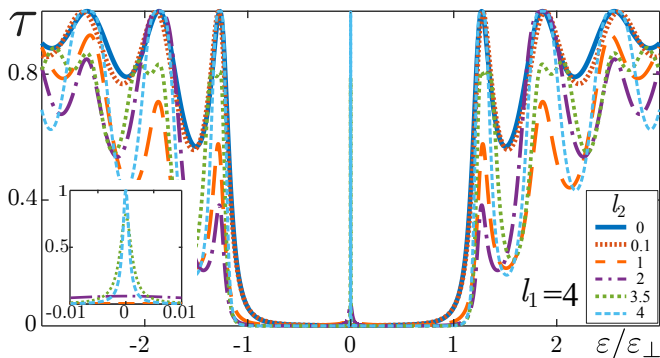


FIG. 10. Transmission function for a two-domain configuration with $\phi = \pi$. The first island has a fixed length and we consider several lengths of the second island. The inset shows a detail of the bound state at zero energy

We see that the transmission function is $\tau = 1$ for $l_1 = l_2$, consistently with our previous analysis of two equally sized domains. For $l_1 \neq l_2$, τ decreases and becomes $\tau \sim 0$ if $l_2 \ll l_1$ (recall that $l_1 > 1$). From Eq. (18) we find that for $|l_1 - l_2| \leq 0.5$ and $l_1 > 1$, τ hosts a clear resonance with $\tau(0) > 0.9$. The behavior of $\tau(\varepsilon)$ for $l_1 \neq l_2$ is illustrated in Fig. 10 for $l_1 = 4$ and $l_2 < l_1$. We see that for $l_1 - l_2 > 2$, the resonance is no longer distinguished within the gap. However, for small difference in the length of the two magnetic domains, not only the resonant peak, but also the behavior of $\tau(\varepsilon)$ above the gap is practically unaffected.

Appendix C ROBUSTNESS OF THE FEATURES OF THE TRANSMISSION FUNCTION AGAINST INHOMOGENEITIES IN THE ORIENTATION OF THE MAGNETIC MOMENT

We now turn to analyze the effect of an inhomogeneity in the orientation of the magnetic moment within each domain. To this end, we divide each magnetic domain in n pieces of the same length, along which the phase gets a random component. Hence, the orientation of the magnetic moment within each of these pieces is $\phi_j = \phi^0 + \delta\phi_j$, $j = 1, \dots, n$, where $\delta\phi_j$ is a random component of the phase within the j -th subdomain, while $\phi^0 = 0, \pi$ for the first and second domain, respectively. According to the previous analysis, the partitions must satisfy $l/n \ll 1$, in order to be considered as a perturbation over the main magnetic configuration of the domain. In fact, for $l/n \sim 1$, each of these partitions would separately open a gap and would behave as an additional magnetic domain.

Examples are shown in Figs. 11 and 12 for weak and strong amplitude in the random component of the magnetic moment, respectively. In each case, we compare the behavior of different numbers of partitions n . In the case of weak disorder shown in Fig. 11, we see that the behavior of the transmission function above the gap is almost unaffected by the inhomogeneous orientation of

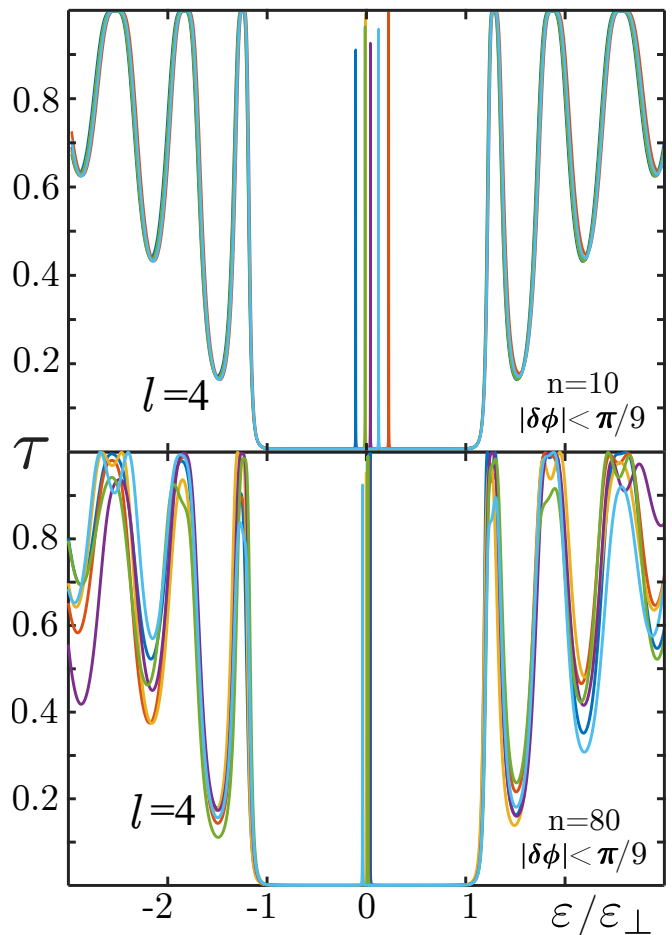


FIG. 11. Transmission function for two domains of equal length $l = 4$ with orientation of the magnetic moments $\phi^0 = 0, \pi$ and random piece-wise random fluctuations $\delta\phi_j = \pm\pi/9$, $j = 1, \dots, n$, within within $n = 10$ partitions of equal length (top) and $n = 80$ (bottom). Different colors correspond to different realizations of disorder.

the magnetic moment, while the position of the resonant peak is slightly shifted away from $\varepsilon = 0$. Albeit, the width of the latter remains unaffected. The shift becomes smaller as the number of partitions increases, as seen in the comparison between the top and bottom panels. The case of strong fluctuations ($\delta\phi_j = \pm 4\pi/9$) is analyzed in Fig. 12. The behavior of the resonance is similar to the case of weak disorder. For increasing fluctuations of the magnetic moment, the shift of the resonance away from $\varepsilon = 0$ is larger. For small number of partitions n (see top panel) the pattern of maxima and minima above the gap becomes also affected. However, the overall structure of $\tau(\varepsilon)$, including the existence of a resonant peak, the clear opening of the gap and a series of peaks with an envelope defined by a Heaviside function are preserved. For larger number of partitions (see bottom panel), all the features, including the resonant peak, as well as the pattern of maxima and minima above the gap are mildly affected.

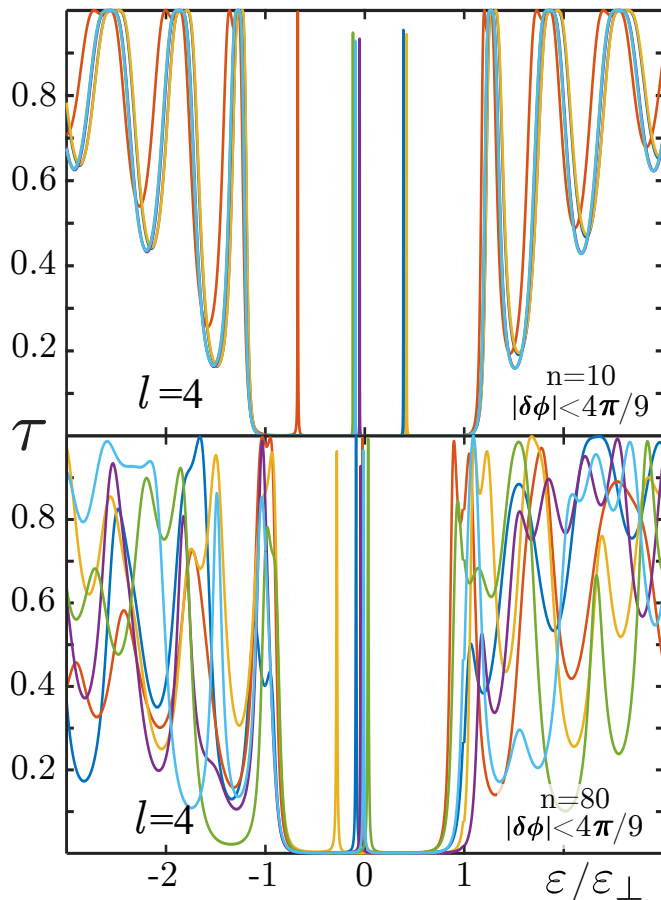


FIG. 12. Same as Fig. 11 with $\delta\phi_j = \pm 4\pi/9$.

The analysis of this and the previous sections lead us to conclude that the performance of the setup is very robust under weak fluctuations in the orientation of the magnetic moment, as well as under fluctuations in the length of the two domains.

-
- [1] F. Giazotto, F., T. T. Heikkilä, A. Luukanen, A. M. Savin, and J.P. Pekola, Opportunities for mesoscopies in thermometry and refrigeration: Physics and applications. *Rev. Mod. Phys.* **78** 2172006 (2006).
- [2] G. Benenti, G. Casati, K. Saito, R. S. Whitney, Fundamental aspects of steady-state conversion of heat to work at the nanoscale, *Phys. Rep.* **694**, 1 (2017).
- [3] J. P. Eisenstein and J. L. Reno, Observation of Chiral Heat Transport in the Quantum Hall Regime, G. Granger, *Phys. Rev. Lett.* **102**, 086803 (2009).
- [4] S. G. Nam, E. H. Hwang and H. J. Lee, Thermoelectric detection of chiral heat transport in graphene in the quantum Hall regime, *Phys. Rev. Lett.* **110** 22680 (2013).
- [5] L. Arrachea and E. Fradkin, Chiral heat transport in driven quantum Hall and quantum spin Hall edge states, *Phys. Rev. B* **84**, 235436 (2011).
- [6] S. Jezouin, F D. Parmentier, A. Anthore, U. Gennser, A. J. Cavanna and F. Pierre, Quantum limit of heat flow across a single electronic channel, *Science* **342** 601 (2013).
- [7] A. Cappelli, M. Huerta, and G. Zemba, Thermal Transport in Chiral Conformal Theories and Hierarchical Quantum Hall States, *Nucl. Phys. B* **636**, 568 (2002).
- [8] E. Grosfeld and S. Das, Probing the Neutral Edge Modes in Transport across a Point Contact via Thermal Effects in the Read-Rezayi Non-Abelian Quantum Hall States, *Phys. Rev. Lett.* **102**, 106403 (2009).
- [9] T. Karzig, G. Refael, L. I. Glazman, F. von Oppen, Energy Partitioning of Tunneling Currents into Luttinger Liquids, *Phys. Rev. Lett.* **107**, 176403 (2011).
- [10] H. Aita, L. Arrachea, C. Naón, and E. Fradkin, Heat transport through quantum Hall edge states: Tunneling versus capacitive coupling to reservoirs, *Phys. Rev. B* **88**, 085122 (2013).
- [11] G. Viola, S. Das, E. Grosfeld, and A. Stern, Thermoelectric probe for neutral edge modes in the fractional quantum Hall regime, *Phys. Rev. Lett.* **109**, 146801 (2012).
- [12] I. Gurman, R. Sabo, M. Heiblum, V. Umansky, and D. Mahalu, Extracting net current from an upstream neutral mode in the fractional quantum Hall regime, *Nature Comm.* **3**, 1289 (2012).
- [13] C. Altimiras, H. le Sueur, U. Gennser, A. Cavanna, D. Mailly and F. Pierre, Tuning energy relaxation along quantum Hall channels, *Phys. Rev. Lett.* **105**, 226804 (2010).
- [14] V. Venkatachalam, S. Hart, L. Pfeiffer, K. West, and A. Yacoby, Local thermometry of neutral modes on the quantum Hall edge *Nature Physics* **8**, 676 (2012).
- [15] A. Cavanna, D. Mailly, and F. Pierre, Chargeless Heat Transport in the Fractional Quantum Hall Regime, C. Altimiras, H. le Sueur, U. Gennser, A. Anthore, *Phys.*

- Rev. Lett. **109**, 026803 (2012).
- [16] M. Banerjee, M. Heiblum, A. Rosenblatt, Y. Oreg, D. E. Feldman, A. Stern, and V. Umansky, Observed quantization of anyonic heat flow, *Nature* **545**, 75 (2017).
- [17] Theory of Disorder-Induced Half-Integer Thermal Hall Conductance D. F. Mross, Y. Oreg, A. Stern, G. Margalit, M. Heiblum, *Phys. Rev. Lett.* **121**, 026801 (2018).
- [18] A. Aharon, Y. Oreg, A. Stern, Phenomenological theory of heat transport in the fractional quantum Hall effect, *Phys. Rev. B* **99**, 041302 (2019).
- [19] R. Sánchez, B. Sothmann, A. N. Jordan, Chiral thermoelectrics with quantum Hall edge states, *Phys. Rev. Lett.* **114**, 146801 (2015).
- [20] P. Samuelsson, S. Kheradsoud, B. Sothmann Optimal quantum interference thermoelectric heat engine with edge states, *Phys. Rev. Lett.* **118**, 256801 (2017).
- [21] S. Kheradsoud, N. Dashti, M. Misiorny, P. P. Potts, J. Splettstoesser, P. Samuelsson, Power, Efficiency and Fluctuations in a Quantum Point Contact as Steady-State Thermoelectric Heat Engine, arXiv:1904.03912.
- [22] L. Vannucci, F. Ronetti, G. Dolcetto, M. Carrega, M. Sassetti, Interference-induced thermoelectric switching and heat rectification in quantum Hall junctions *Phys. Rev. B* **92**, 075446 (2015).
- [23] P. Roura-Bas, L. Arrachea, E. Fradkin, Enhanced thermoelectric response in the fractional quantum Hall effect *Phys. Rev. B* **97**, 081104 (2018).
- [24] A Xiao-Qin Yu, Zhen-Gang Zhu, Gang Su, A. -P. Jauho, spin caloritronic battery, *Phys. Rev. Applied* **8**, 054038 (2017).
- [25] Flavio Ronetti, Luca Vannucci, Giacomo Dolcetto, Matteo Carrega, Maura Sassetti, Spin-thermoelectric transport induced by interactions and spin-flip processes in two dimensional topological insulators, *Phys. Rev. B* **93**, 165414 (2016).
- [26] Sun-Yong Hwang, Rosa Lopez, Minchul Lee, David Sanchez, Nonlinear spin-thermoelectric transport in two-dimensional topological insulators, *Phys. Rev. B* **90**, 115301 (2014).
- [27] Po-Hao Chang, Mohammad Saeed Bahramy, Naoto Nagaosa, Branislav K. Nikolic Giant thermoelectric effect in graphene-based topological insulators with nanopores, *Nano Lett.* **14**, 3779 (2014).
- [28] D. G. Rothe, E. M. Hankiewicz, B. Trauzettel, M. Guigou, Spin-dependent thermoelectric transport in HgTe/CdTe quantum wells, *Phys. Rev. B* **86**, 165434 (2012).
- [29] P. Roura-Bas, L. Arrachea, and E. Fradkin, Helical spin thermoelectrics controlled by a side-coupled magnetic quantum dot in the quantum spin Hall state, *Phys. Rev. B* **98**, 195429 (2018).
- [30] D. Sanchez, R. Sanchez, R. Lopez, B. Sothmann, Nonlinear chiral refrigerators, arXiv:1904.04506.
- [31] Arjun Mani, Colin Benjamin, Helical thermoelectrics and refrigeration, *Phys. Rev. E* **97**, 022114 (2018).
- [32] C. L. Kane and E. J. Mele, Z_2 Topological Order and the Quantum Spin Hall Effect, *Phys. Rev. Lett.* **95**, 146802 (2005).
- [33] C. L. Kane and E. J. Mele, Quantum Spin Hall Effect in Graphene, *Phys. Rev. Lett.* **95**, 226801 (2005).
- [34] B. A. Bernevig, T. L. Hughes, and S.-C. Zhang, Quantum Spin Hall Effect and Topological Phase Transition in HgTe Quantum Wells, *Science* **314**, 1757 (2006).
- [35] M. König, S. Wiedmann, C. Brüne, A. Roth, H. Buhmann, L. W. Molenkamp, X. L. Qi, and S.-C. Zhang, Quantum Spin Hall Insulator State in HgTe Quantum Wells, *Science* **318**, 766 (2007).
- [36] A. Roth, C. Brüne, H. Buhmann, L. W. Molenkamp, J. Maciejko, X-L. Q, S-C Zhang, Nonlocal Transport in the Quantum Spin Hall State *Science* **325**, 294 (2009).
- [37] C. Brüne, A. Roth, H. Buhmann, E. M. Hankiewicz, L. W. Molenkamp, J. Maciejko, X-L. Qi, and S-C. Zhang, Spin polarization of the quantum spin Hall edge states *Nature Phys.* **8**, 485 (2012).
- [38] B. J. van Wees, H. van Houten, C. W. J. Beenakker, J. G. Williamson, L. P. Kouwenhoven, D. van der Marel, C. T. Foxon, Quantized conductance of point contacts in a two-dimensional electron gas. *Phys. Rev. Lett.* **60**, 848 (1988).
- [39] H. van Houten, L. W. Molenkamp, C. W. J. Beenakker, C.T. Foxon, Thermoelectric properties of quantum point contacts. *Semicond. Sci. Technol.* **7**, B215 (1992).
- [40] M. Büttiker, Quantized transmission of a saddle-point constriction. *Phys. Rev. B* **41**, 7906 (1990).
- [41] J. Strunz, J. Wiedenmann, C. Fleckenstein, L. Lunczer, W. Beugeling, V. L. Müller, P. Shekhar, N. Traverso Ziani, S. Shamim, J. Kleinlein, H. Buhmann, B. Trauzettel, L. W. Molenkamp, Interacting topological edge channels, arXiv:1905.08175.
- [42] F. Dolcini, Full electrical control of charge and spin conductance through interferometry of edge states in topological insulators, *Phys. Rev. B* **83**, (2011).
- [43] P. Virtanen, P. Recher, Dephasing of spin and charge interference in helical Luttinger liquids, *Phys. Rev. B* **83**, 115332 (2011)
- [44] F. Romeo, R. Citro, D. Ferraro and M. Sassetti, Electrical switching and interferometry of massive Dirac particles in topological insulator constrictions, *Phys. Rev. B* **86**, 165418 (2012).
- [45] B. Rizzo, L. Arrachea, M. Moskalets, Transport phenomena in helical edge states interferometers. A Green's function approach, *Phys Rev B* **88**, 155433 (2013).
- [46] F. Crépin, J. C. Budich, F. Dolcini, P. Recher, and B. Trauzettel, Renormalization group approach for the scattering off a single Rashba impurity in a helical liquid, *Phys. Rev. B* **86**, 121106 (R) (2012).
- [47] G. Dolcetto, F. Cavaliere, D. Ferraro, and M. Sassetti, Generating and controlling spin-polarized currents induced by a quantum spin Hall antidot, *Phys. Rev. B* **87**, 085425 (2013).
- [48] K. T. Law, C. Y. Seng, Patrick A. Lee, and T. K. Ng, Quantum dot in a two-dimensional topological insulator: The two-channel Kondo fixed point *Phys. Rev. B* **81**, 041305 (2010).
- [49] T. Posske, C-X Liu, J. C. Budich, and B. Trauzettel, Exact Results for the Kondo Screening Cloud of Two Helical Liquids, *Phys. Rev. Lett.* **110**, 016602 (2013).
- [50] B. Probst, P. Virtanen, P. Recher, Controlling spin polarization of a quantum dot via a helical edge state, *Phys. Rev. B* **92**, 045430 (2015).
- [51] B. Rizzo, A. Camjayi, Liliana Arrachea Transport in quantum spin Hall edges in contact to a quantum dot *Phys. Rev. B* **94**, 125425 (2016).
- [52] G. D. Mahan, J. O. Sofo, The best thermoelectric. *Proc. Natl. Acad. Sci. U.S.A.* **93**, 7436 (1996).
- [53] G. Benenti, K. Saito, and G. Casati, Thermodynamic Bounds on Efficiency for Systems with Broken Time-Reversal Symmetry, *Phys. Rev. Lett.* **106**, 230602 (2011).

- [54] R. S. Whitney, Most Efficient Quantum Thermoelectric at Finite Power Output. *Phys. Rev. Lett.* **112**, 130601 (2014) .
- [55] R. S. Whitney, Finding the quantum thermoelectric with maximal efficiency and minimal entropy production at given power output, *Phys. Rev. B* **91**, 115425 (2015).
- [56] M. Josefsson, A. Svilans, A. M. Burke, E. A. Hoffmann, S. Fahlvik, C. Thelander, M. Leijnse, H. Linke, A quantum-dot heat engine operating close to the thermodynamic efficiency limits, *Nat. Nanotechnol.* **13**, 920 (2018).
- [57] P. A. Erdman, F. Mazza, R. Bosisio, G. Benenti, R. Fazio, Fabio Taddei Thermoelectric properties of an interacting quantum dot-based heat engine *Phys. Rev. B* **95**, 245432 (2017).
- [58] D. Prete, Paolo A. Erdman, V. Demontis, V. Zannier, D. Ercolani, L. Sorba, F. Beltram, F. Rossella, F. Taddei, S. Roddaro, Thermoelectric conversion at 30K in InAs/InP nanowire quantum dots, arXiv:1903.06935.
- [59] B. Dutta, J. T. Peltonen, D. S. Antonenko, M. Meschke, M. A. Skvortsov, B. Kubala, J. König, C. B. Winkelmann, H. Courtois, and J. P. Pekola, Thermal Conductance of a Single-Electron Transistor, *Phys. Rev. Lett.* **119**, 077701 (2017).
- [60] O. Entin-Wohlman, Y. Imry and A. Aharony, Enhanced performance of joint cooling and energy production, *Phys. Rev. B* **91**, 054302 (2015).
- [61] D. Pérez Daroca, P. Roura-Bas, A. A. Aligia, Enhancing of nonlinear thermoelectric response of a correlated quantum dot in the Kondo regime by asymmetrically coupling to the leads, *Phys. Rev. B* **97**, 165433 (2018)
- [62] D. B. Karki, M. N. Kiselev, Exceeding quantum upper bound of power production in nano devices: effects of resonance scattering and strong electron interactions, arXiv:1906.00724
- [63] Q. Meng, S. Vishveshwara, T. L. Hughes, Spin-transfer torque and electric current in helical edge states in quantum spin Hall devices, *Phys. Rev. B* **90**, 205403 (2014).
- [64] L. Arrachea and F. von Oppen, Nanomagnet coupled to quantum spin Hall edge: An adiabatic quantum motor, *Physica E* **74**, 596 (2015).
- [65] P. G. Silvestrov, P. Recher, P. W. Brouwer, Noiseless manipulation of helical edge state transport by a quantum magnet, *Phys. Rev. B* **93**, 205130 (2016).
- [66] L. Fu and C. L. Kane, Josephson current and noise at a superconductor/quantum-spin-Hall-insulator/superconductor junction *Phys. Rev. B* **79**, 161408 (2009).
- [67] M. Houzet, J. S. Meyer, D. M. Badiane, and L. I. Glazman, Dynamics of Majorana States in a Topological Josephson Junction *Phys. Rev. Lett.* **111**, 046401 (2013).
- [68] Francois Crépin, Björn Trauzettel, and Fabrizio Dolcini, Signatures of Majorana bound states in transport properties of hybrid structures based on helical liquids, *Phys. Rev. B* **89**, 205115 (2014).
- [69] R. Bustos-Marun, G. Refael, and F. von Oppen, Adiabatic Quantum Motors, *Phys. Rev. Lett.* **111**, 060802 (2013).
- [70] Jackiw, R. and Rebbi, C. Solitons with fermion number. *Phys. Rev. D* **13**, 3398 (1976).
- [71] Su, W. P., Shrieffer, J. R. and Heeger, A. J. Soliton excitations in polyacetylene. *Phys. Rev. B* **22**, 2099 (1980).
- [72] See supplementary material for details on the behavior of the maximum power for the heat engine and the figure of merit of reference transmission functions.
- [73] G. Scheunert, O. Heinonen, R. Hardeman, A. Lapicki, M. Gubbins, and R. M. Bowman, A review of high magnetic moment thin films for microscale and nanotechnology applications. *Appl. Phys. Rev.* **3**, 011301,(2016).